Chemical Science

ROYAL SOCIETY OF CHEMISTRY

EDGE ARTICLE

View Article Online
View Journal | View Issue

Cite this: *Chem. Sci.*, 2026, **17**, 8504

All publication charges for this article have been paid for by the Royal Society of Chemistry

Received 14th February 2026
Accepted 5th March 2026

DOI: 10.1039/d6sc01336h

rsc.li/chemical-science

Engineering the interfacial water microenvironment to accelerate proton transfer for acidic oxygen evolution at high-potential

Xiaolong Liang,[a] Ke Xu,[a] Hengkun Yu,[a] Xu Ge,[a] Zhiwen Liu,[a] Xueliang Mu,[d] Shaoke Zhang,[b] Jake M. Yang[c] and Jinxuan Liu*[ade]

Proton transfer (PT) kinetics through the electric double layer is a critical yet often overlooked bottleneck for acidic oxygen evolution reaction (OER) under industrially relevant high potential conditions. Herein, we propose an interfacial water microenvironment engineering strategy to address this challenge by constructing a CdO–$Co_{3-x}Cd_xO_4$ heterostructure with a strong built-in electric field. Combined *in situ* ATR-SEIRAS, kinetic isotope effect (KIE) analysis, and *ab initio* molecular dynamics (AIMD) simulations reveal that the induced electric field effectively disrupts the rigid interfacial hydrogen-bond network, increasing the proportion of isolated water molecules. Crucially, this disordered water structure significantly lowers the energy barrier for water reorientation, thereby directly accelerating the rate-determining proton transfer kinetics. As a result, the catalyst exhibits an order-of-magnitude enhancement in intrinsic activity at 1.70 V *vs.* RHE compared to pure Co_3O_4. This work establishes the rational engineering of the interfacial H-bond network as a decisive strategy for overcoming the kinetic limitations of high-potential electrocatalysis.

Introduction

The transition to a sustainable energy future relies heavily on the advancement of green hydrogen production technologies.[1–3] Proton exchange membrane water electrolysis (PEMWE) represents a promising pathway for efficient hydrogen generation, offering distinct advantages such as rapid dynamic response, high current density operation, and compact system design.[4–7] Nonetheless, the widespread deployment of PEMWE is fundamentally constrained by the sluggish kinetics of the anodic oxygen evolution reaction (OER) in acidic media. While noble metal oxides like IrO_2 and RuO_2 set the benchmark for activity, their scarcity and high cost prohibit terawatt-scale application.[8–10] Consequently, developing robust, cost-effective alternatives based on earth–abundant transition metals—particularly cobalt-based spinel oxides—has become a central imperative in modern electrocatalysis.[11] Moreover, the binding energy of metallic cadmium (Cd) for oxygen intermediates is weak, which allows the surface of a heterogeneous interface to be balanced for catalyst performance.[12]

For decades, the design of acidic OER catalysts has been dominated by a "solid-centric" paradigm. Researchers have focused extensively on optimizing the intrinsic electronic structure of the solid catalyst—such as modulating the d-band center or adjusting the metal–oxygen covalency—to tailor the binding energies of reaction intermediates (*O, *OH, and *OOH) towards the structure–activity relationship.[13,14] Strategies including elemental doping, defect engineering, and strain manipulation have successfully lowered the activation barriers for surface adsorption steps.[15–18] However, as OER electrocatalysts are pushed towards industrially relevant high-current-density regimes, a new kinetic bottleneck emerges that electronic optimization alone cannot resolve: the transport of protons. At high anodic potentials, the rapid generation of protons necessitates their efficient removal from the catalyst surface through the electric double layer (EDL) to the bulk electrolyte.[19,20]

According to the Grotthuss mechanism, this proton transport is heavily reliant on the rapid reorientation and hydrogen-bond (H-bond) dynamics of interfacial water molecules.[21] Recent mechanistic studies suggest that the structure of interfacial water within the EDL plays a decisive, yet frequently overlooked, role in governing these proton transfer kinetics. For instance, Li *et al.* demonstrated that the connectivity of the H-bond network within the EDL dominates the kinetic pH effect in hydrogen electrocatalysis.[2] Similarly, other studies have

[a]*State Key Laboratory of Fine Chemicals, Dalian University of Technology, 116024 Dalian, China*

[b]*Advanced Institute for Ocean Research, Southern University of Science and Technology, 1088, Xueyuan Blvd., Nanshan District, Shenzhen, Guangdong, P. R. China*

[c]*Centre for Sustainable Materials Processing, School of Chemistry, University of Leicester, University Road, Leicester, LE1 7RH, UK*

[d]*Leicester International Institute, State Key Laboratory of Fine Chemicals, Dalian University of Technology, 116024 Dalian, China. E-mail: jinxuan.liu@dlut.edu.cn*

[e]*Liaoning Binhai Laboratory, 116023 Dalian, China*

shown that a rigid, highly ordered water layer at the electrode–electrolyte interface creates a substantial energy barrier for water reorientation, thereby severely hindering proton transfer.[22–24] There remains a scarcity of strategies that intrinsically engineer the solid catalyst surface to perturb the interfacial liquid structure actively.

Herein, we propose that constructing a heterostructure with a strong built-in electric field can serve as a potent tool to physically perturb the interfacial aqueous network. However, direct experimental evidence correlating such field-induced H-bond disruption with enhanced proton transfer kinetics in acidic OER is still lacking. We present a paradigm shift by establishing the integrity of the interfacial hydrogen-bond network as a critical kinetic determinant regulating acidic OER activity. We strategically engineered a CdO–$Co_{3-x}Cd_xO_4$ heterostructure as a model system to investigate this interfacial physics. The distinct electronic contrast between CdO and Co_3O_4 induces a strong interfacial electric field, which serves as a "switch" to modulate the local water structure. By integrating *in situ* electrochemical impedance spectroscopy (EIS), attenuated total reflection surface-enhanced infrared absorption spectroscopy (ATR-SEIRAS), and *ab initio* molecular dynamics (AIMD) simulations, we decouple the interfacial water dynamics from bulk catalytic properties. Our investigation reveals a mechanism: the heterostructure induces a severe disruption of the rigid H-bond network at high potentials, creating an environment rich in isolated water molecules. Crucially, kinetic isotope effect (KIE) studies unambiguously confirm that this structural perturbation accelerates the rate-determining proton transfer step. These findings demonstrate that overcoming the kinetic bottlenecks of water splitting requires a focus: simultaneous optimization of the solid catalyst's electronic structure and the liquid electrolyte's interfacial network.

Results and discussion

The pursuit of industrially relevant current densities necessitates evaluating OER catalysts at high anodic potentials. We began by first synthesizing Co/Cd heterogeneous catalysts *via* electrodeposition of different ratios of dissolved Co and Cd onto carbon paper (CP) with an applied current density of −20 mA cm^{-1-2} for a duration of 10 minutes. Next, a systematic investigation of the electrochemical performance of the synthesized Co/Cd heterostructure catalysts was performed in 0.5 M H_2SO_4. Fig. S2 shows the linear sweep voltammetry (LSV) curves. As can be seen, all Co/Cd heterostructure catalysts exhibited superior catalytic activity towards the OER compared to their single-phase catalysts (Fig. S2). Based on the observed overpotential at a 10 mA cm^{-2} current density, the optimal Co/Cd heterostructure catalyst was derived from an electrodeposition process containing dissolved Co and Cd at a ratio of 7 : 3. For simplicity, this catalyst is named CdO–$Co_{3-x}Cd_xO_4$/CP in the rest of this work.

The most striking phenomenon emerged from a potential-resolved activity analysis. While the optimal heterostructure (CdO–$Co_{3-x}Cd_xO_4$/CP, as above) showed only a modest current density advantage of 12 mA cm^{-2} over Co_3O_4/CP at 1.6 V, this performance gap was dramatically amplified by an order of magnitude to 125 mA cm^{-2} at 1.7 V (Fig. 1a). This gap even reached 334 mA at 1.75 V. Quantitatively, at a high anodic potential of 1.70 V *vs.* RHE, CdO–$Co_{3-x}Cd_xO_4$/CP exhibits a remarkable specific activity of 7.5 mA cm^{-2}, which is approximately 1.6 times higher than that of the pristine Co_3O_4/CP (4.2 mA cm^{-2}). This profound potential-dependence signifies a fundamental shift in the operative reaction kinetics at high potentials, a phenomenon that conventional critical factors based solely on the solid catalyst's electronic structure are inadequate to explain.

Further kinetic analysis *via* Tafel plots (Fig. 1b) yielded a slope of 81.2 mV dec^{-1} for CdO–$Co_{3-x}Cd_xO_4$/CP, significantly lower than the 102.6 mV dec^{-1} for Co_3O_4/CP. The smaller Tafel slope indicates more favorable reaction kinetics and a faster increase in the OER rate with applied overpotential. More importantly, the difference in the Tafel slope indicates that the heterostructure may have altered or optimized the rate-determining step of the reaction. Moreover, the electrochemical active surface area (ECSA), estimated from the double-layer capacitance (C_{dl}), was found to be substantially larger for CdO–$Co_{3-x}Cd_xO_4$/CP (9.27 mF cm^{-2}) than for Co_3O_4/CP (4.03 mF cm^{-2}) (Fig. S5 and S6). This significantly increased C_{dl} value is usually attributed to the increase in the electrochemical active area. To decouple the intrinsic activity from the effect of surface

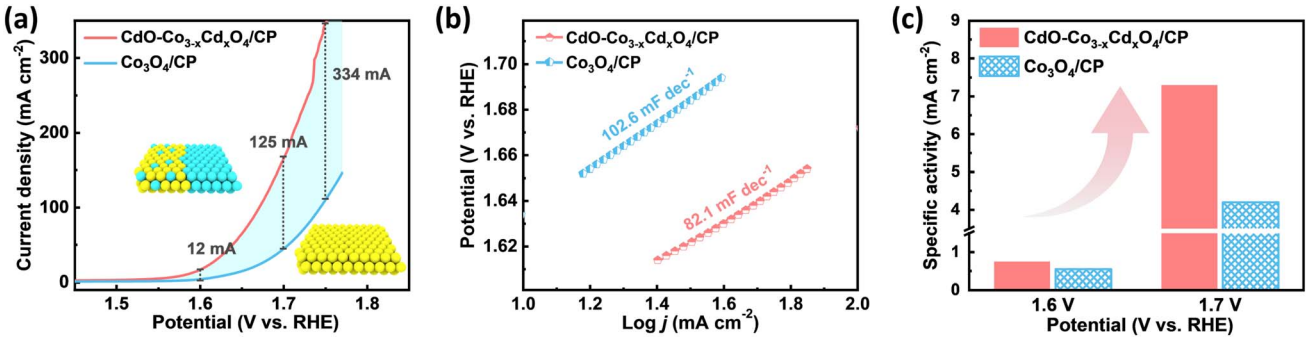

Fig. 1 (a) LSV curves of CdO–$Co_{3-x}Cd_xO_4$/CP and Co_3O_4/CP in 0.5 M H_2SO_4, (b) corresponding Tafel plots according to the LSV curves, and (c) specific activities (ECSA-normalized current density) of CdO–$Co_{3-x}Cd_xO_4$/CP and Co_3O_4/CP.

area, the current densities were normalized by the electrochemically active surface area (ECSA). The CdO–$Co_{3-x}Cd_xO_4$/CP catalyst showed superior performance in terms of specific activity (ECSA-normalized current density) to Co_3O_4/CP, consistent with the trend observed in the LSV measurements. We propose that it may also reflect the enhanced interfacial interaction between the heterointerface and the electrolyte and the alteration of the interfacial double-layer structure, which provides preliminary electrochemical evidence for the subsequent discussion on the reconstruction of the interfacial water structure.

Having established the potential-dependent OER performance, we characterize the structural and electronic properties of the CdO–$Co_{3-x}Cd_xO_4$/CP and Co_3O_4/CP catalysts. X-ray diffraction (XRD) analysis (Fig. 2a and S7) confirmed the successful formation of the heterostructure. As shown in Fig. S8, the diffraction peaks of carbon paper at 2θ values of 26.4° and 54.5° (PDF#41-1487) remained intact after the electrodeposition process, indicating that the structural integrity of the carbon paper was not compromised. The diffraction peaks observed at 19.0°, 31.3°, 36.8°, 38.5°, 44.8°, 55.6°, 59.3°, and 65.2° correspond to the (111), (220), (311), (222), (400), (422), (511), and (440) crystallographic planes of the Co_3O_4 spinel (PDF#43-1003), while new peaks emerging at 33.0° and 38.2° were attributed to the CdO phase (PDF#05-0640). It is worth noting that with the doping of Cd, the characteristic diffraction peaks of Co_3O_4 systematically shift towards a low angle (inset in Fig. S9), which clearly indicates that Cd^{2+} has been successfully introduced into the Co_3O_4 lattice, forming a $Co_{3-x}Cd_xO_4$ solid solution, thereby establishing a tight heterointerface between CdO and Co_3O_4.

The chronopotentiometry test (Fig. S11) further confirmed the stability of the CdO–$Co_{3-x}Cd_xO_4$/CP catalyst, which exhibited stable operation for 90 hours at 10 mA cm^{-2}, far exceeding the performance of Co_3O_4/CP. Post-test characterization by XRD and SEM confirmed the structural and morphological integrity of the catalyst (Fig. S12 and S13).

Raman spectroscopy was employed to investigate the lattice dynamics of the Co/Cd catalysts with varying ratios. As illustrated in Fig. 2b and S14, five typical Raman-active modes, specifically A_{1g}, E_g, and three F_{2g} modes, are characteristic of cubic spinel oxides.[25] The A_{1g} mode is associated with Co^{3+}–O stretching in the octahedral CoO_6 unit, while the F_{2g} mode pertains to Co^{2+}–O stretching in the tetrahedral CoO_4 geometry. The A_{1g} mode in CdO–$Co_{3-x}Cd_xO_4$ (655.4 cm^{-1}) exhibits a red shift relative to Co_3O_4 (Fig. 1c), which is attributed to the presence of oxygen vacancies that increase lattice disorder.[26] The generation of such lattice distortions and defects is the key to inducing local built-in electric fields and interface forces and is regarded as the initial driving force for regulating the interface microenvironment.[27]

Electron microscopy provided direct visual evidence of the heterostructure. High-resolution transmission electron microscopy (HR-TEM) and fast Fourier transform (FFT) analyses indicated that the CdO–$Co_{3-x}Cd_xO_4$ composite material had a polycrystalline structure and was scattered with amorphous

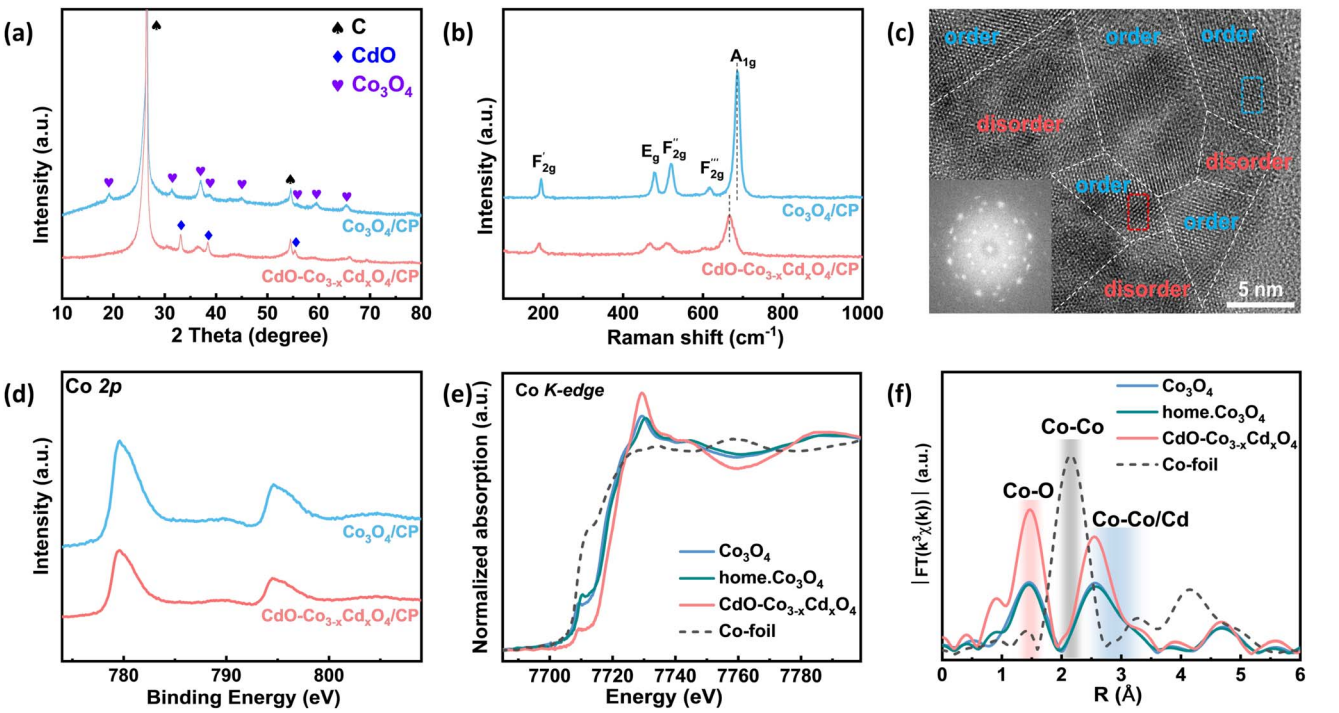

Fig. 2 (a) XRD patterns of CdO–$Co_{3-x}Cd_xO_4$/CP and Co_3O_4. (b) Raman spectrum of CdO–$Co_{3-x}Cd_xO_4$ and Co_3O_4. (c) HRTEM image of CdO–$Co_{3-x}Cd_xO_4$. The insets show the FFT patterns of the selected areas. (d) High-resolution Co 2p XPS spectra of CdO–$Co_{3-x}Cd_xO_4$/CP and Co_3O_4/CP. (e) Normalized XANES spectra at the Co K-edge of CdO–$Co_{3-x}Cd_xO_4$ and Co_3O_4, and Co foil which were used as references. (f) EXAFS spectra of CdO–$Co_{3-x}Cd_xO_4$ and Co_3O_4.

regions (Fig. 2c). It is worth noting that the observed 0.25 nm interplanar spacing corresponds to the (311) crystal plane of $Co_{3-x}Cd_xO_4$ and is slightly larger than the 0.24 nm interplanar spacing of the (311) crystal plane of single-phase Co_3O_4 (Fig. S15 and S16). This observation indicates that the incorporation of Cd leads to lattice distortion in the Co_3O_4 structure, confirming the lattice expansion observed by XRD. Moreover, from Fig. 2c, it is found that there are obvious grain boundaries and locally ordered regions in CdO–$Co_{3-x}Cd_xO_4$, which also proves that a heterointerface is constructed between CdO and Co_3O_4. Fig. S17 and S18 show the scanning electron microscope (SEM) images of the CdO–$Co_{3-x}Cd_xO_4$ and Co_3O_4 catalysts. Furthermore, Fig. S19–S21 illustrate the distribution of elements in the catalyst, with no significant leaching of elements observed after the OER (Fig. S22).

The electronic structure of the heterostructure catalysts was systematically investigated through X-ray photoelectron spectroscopy (XPS) and X-ray absorption near edge structure (XANES) analyses. High-resolution XPS spectra revealed distinct Co 2p doublet peaks at 779.8 eV ($2p_{3/2}$) and 794.8 eV ($2p_{1/2}$),[28] along with Cd 3d signals at 405.2 eV ($3d_{5/2}$) and 412.1 eV ($3d_{3/2}$), consistent with characteristic spin-orbit transitions (Fig. 2d).[29] This observation, combined with the shift of the Co K-edge in CdO–$Co_{3-x}Cd_xO_4$ to higher energies compared to Co_3O_4 (Fig. 2e), indicates an elevated oxidation state of Co in the heterostructure catalyst, providing direct evidence of interfacial electron transfer. This transfer of electrons from CdO to $Co_{3-x}Cd_xO_4$ generates an internal electric field at the heterointerface, which is a key electronic factor in regulating the charge distribution at the interface and influencing the adsorption orientation of water molecules. Extended X-ray absorption fine structure (EXAFS) revealed two prominent coordination shells at 1.47 Å and 2.54 Å, corresponding to Co–O and Co–Co/Cd coordination environments (Fig. 2f). The slight rightward shift of these peaks relative to Co_3O_4 indicates lattice distortion after Cd incorporation, corroborating the XRD observations. Further characterization through wavelet transform (WT) analysis resolved distinct coordination features: intensity maxima at (6 $Å^{-1}$, 1.5 Å) and (~6 $Å^{-1}$, 2.5 Å) correspond to Co–O and Co–Co/Cd coordination, while the feature at (8 $Å^{-1}$, 2.2 Å) arises from Co–Co coordination (Fig. S24). These WT-derived coordination parameters show excellent agreement with conventional EXAFS analysis. These findings collectively demonstrate pronounced electronic interactions between CdO and $Co_{3-x}Cd_xO_4$ at the heterointerface, enhancing the interfacial influence on electrolyte interactions. This interfacial electron rearrangement not only regulates the valence state of Co, but more importantly, generates a significant dipole moment or local electric field at the interface, which provides an electrostatic driving force for the subsequent destruction of the interfacial water structure.

To directly validate our hypothesis that the heterointerface modulates the interfacial water structure, we employed a combination of *operando* electrochemical and spectroscopic techniques. We first utilized electrochemical impedance spectroscopy (EIS) to probe the potential-dependent properties of the electrode–electrolyte interface. Tests are conducted within the frequency range of 10^{-1} to 10^4 Hz. The Nyquist plots for CdO–$Co_{3-x}Cd_xO_4$/CP and Co_3O_4/CP at various potentials are shown in Fig. 3a and S25. The impedance semicircle for both catalysts decreased with increasing potential, indicating accelerated reaction kinetics.[30] To further investigate the variations in *operando* EIS, equivalent circuit diagrams were constructed, as shown in Fig. S26. Here, R_s represents the solution resistance while R_{ct} and R–OH correspond to the charge transfer resistance and the resistance associated with intermediate accumulation, respectively. CPE and CPE–OH denote the double layer capacitor and the adsorption coverage of the hydroxyl (*OH) intermediates. The results from the fitting analysis are presented in Fig. 3c and S27, where trends in R–OH and CPE–OH reveal the evolution of hydroxyl species on the catalyst surface during the OER. Notably, a smaller sum of R_{ct} and R–OH indicates faster charge transfer kinetics. As shown in Fig. S27a and S27c, the resistance of CdO–$Co_{3-x}Cd_xO_4$/CP remains consistently lower than that of the single-phase Co_3O_4/CP at all potentials, suggesting that the kinetics of *OH ion adsorption is more favorable during the OER process.[31] Conversely, the accelerated accumulation of *OH ions facilitated by the larger constant phase element (CPE) likely enhances the overall catalytic performance.[32] At all potentials, CdO–$Co_{3-x}Cd_xO_4$/CP exhibits a higher CPE-OH compared to Co_3O_4/CP, indicating greater *OH coverage on the CdO–$Co_{3-x}Cd_xO_4$/CP surface (Fig. S26b). This rapid accumulation of *OH on CdO–$Co_{3-x}Cd_xO_4$/CP is advantageous for catalysis.[31] We interpret this dramatically enhanced CPE and CPE-OH not merely as higher intermediate coverage, but as a direct electrochemical signature of a more flexible and responsive EDL structure. This increased interfacial capacitance implies that the heterostructure interface can undergo more extensive restructuring under potential perturbation, creating an environment conducive to interface water reorganization. The significantly enhanced capacitance indicates a more dynamic and polarizable double-layer structure, which is conducive to the reorganization of water molecules for rapid proton transfer.

The Bode plot, which depicts phase angle as a function of frequency, reflects the dynamic evolution of the electrocatalysts during the OER. As illustrated in Fig. 4b and S28–S29, the Bode phase diagrams for both CdO–$Co_{3-x}Cd_xO_4$/CP and Co_3O_4/CP reveal two peaks in different frequency ranges. The peak in the mid-frequency region (10^2–10^3 Hz) corresponds to surface bilayer capacitance, while the peak in the low-frequency range (10^0–10^1 Hz) is associated with the OER response.[33] Critically, with increasing potential, the low-frequency peak for CdO–$Co_{3-x}Cd_xO_4$/CP decreased in magnitude and shifted to higher frequencies more rapidly than that for Co_3O_4/CP. This indicates a faster interfacial reaction rate and a reduction in the time constant for the OER.[34,35] Furthermore, the peaks of the heterostructure CdO–$Co_{3-x}Cd_xO_4$/CP transition to higher frequencies more rapidly at elevated potentials. This result is attributed to the low energy barrier in the rate-determining step, which is consistent with promoting proton transfer.[36,37]

The variation of interfacial water distribution will affect the hydrogen bond network, making it a key factor in catalytic activity.[38,39] To obtain interfacial water molecular-level evidence,

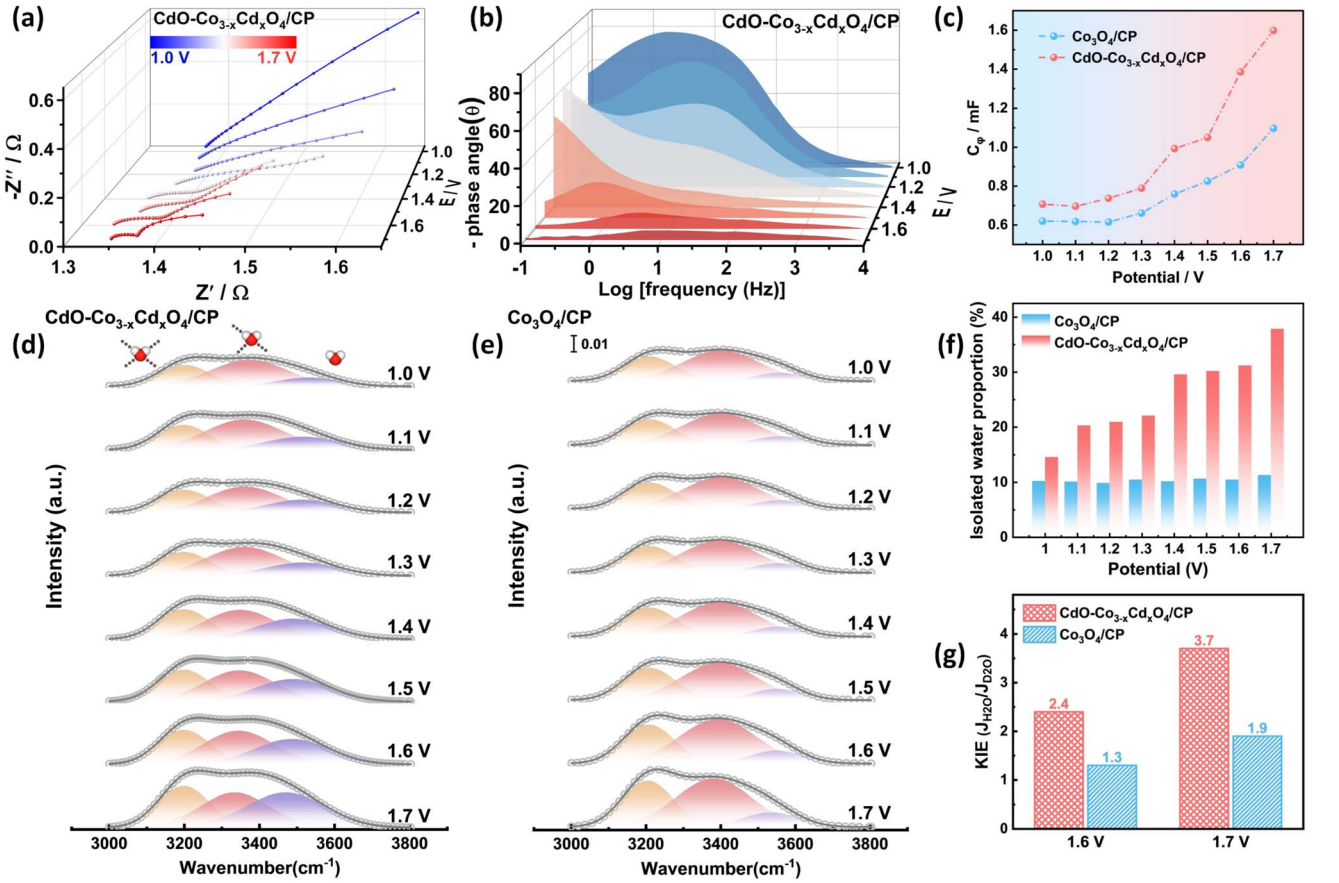

Fig. 3 (a) The Nyquist plots of CdO–$Co_{3-x}Cd_xO_4$/CP at different applied potentials. (b) Bode phase plots of CdO–$Co_{3-x}Cd_xO_4$/CP at different applied potentials. (c) The extracted CPE plots of CdO–$Co_{3-x}Cd_xO_4$P at different applied potentials. (d and e) *In situ* ATR-SEIRAS spectra recorded between 3000 and 3800 cm^{-1} on CdO–$Co_{3-x}Cd_xO_4$ and Co_3O_4 at different applied potentials. (f) The OH stretching bands of isolated O–H of CdO–$Co_{3-x}Cd_xO_4$ and Co_3O_4 determined by Gaussian fitting denoted in red and blue, respectively. (g) Comparison of KIE data of CdO–$Co_{3-x}Cd_xO_4$/CP and Co_3O_4/CP at different applied potentials.

we conducted *operando* ATR-SEIRAS to monitor the –OH stretching band of interfacial water (3000–3800 cm^{-1}) at applied potentials (Fig. 3d, e, Tables S4 and S5).[40–42] This band was deconvoluted into three components assigned to tetra-coordinated (strong H-bond), tri-coordinated (medium H-bond), and isolated (weak H-bond) water molecules. Utilizing the Stark effect, variations in OH stretching at different applied potentials can provide insights into the structural changes and the number of hydrogen bonds within the interfacial water. Essentially, the proximity of weakly hydrogen-bonded water to the electrode surface is crucial for determining the water decomposition capacity.[43] Although the traditional four-coordinated water network is stable, it restricts the re-orientation of water molecules. In contrast, isolated water networks can lower the reorientation energy barrier, thereby accelerating proton transfer. Strikingly, the proportion of isolated water on the CdO–$Co_{3-x}Cd_xO_4$ surface exhibited a strong potential-dependent increase, significantly surpassing that on Co_3O_4 at high potentials (Fig. 3d and e). To quantify the disruption of interface water, we calculated the proportion of isolated water (Fig. 3f). The results clearly indicate that for the heterostructure CdO–$Co_{3-x}Cd_xO_4$, with the increase of potential, the proportion of isolated water increases rapidly, rising from 15 to 47%, while the proportion of isolated water on the Co_3O_4 surface remains virtually unchanged. This also indicates that the heterostructure disrupts the connectivity of the hydrogen bond network, increases the mobility of protons at high potentials, and enhances the water splitting capacity. And Fig. S30 plots the current density at 1.7 V against the proportion of isolated water for both catalysts; a clear positive correlation emerged. This direct correlation establishes a robust link between the microscopic structure of interfacial water and the macroscopic electrocatalytic activity, strongly supporting the proposed critical factor.

To rigorously verify that the disrupted interfacial H-bond network indeed accelerates the reaction kinetics by facilitating proton transport, we conducted KIE experiments by substituting H_2O with D_2O. Since the O–D bond is stronger and has a lower zero-point energy than the O–H bond, replacing protium with deuterium significantly retards reaction steps involving proton transfer (PT) or proton-coupled electron transfer (PCET), serving as a sensitive probe for the rate-determining step (RDS). As shown in Fig. S31, both CdO–$Co_{3-x}Cd_xO_4$/CP and Co_3O_4/CP exhibit a palpable decrease in OER current density in the deuterated electrolyte, yielding KIE values (j_{H_2O}/j_{D_2O}) greater than 1.[44] This observation confirms

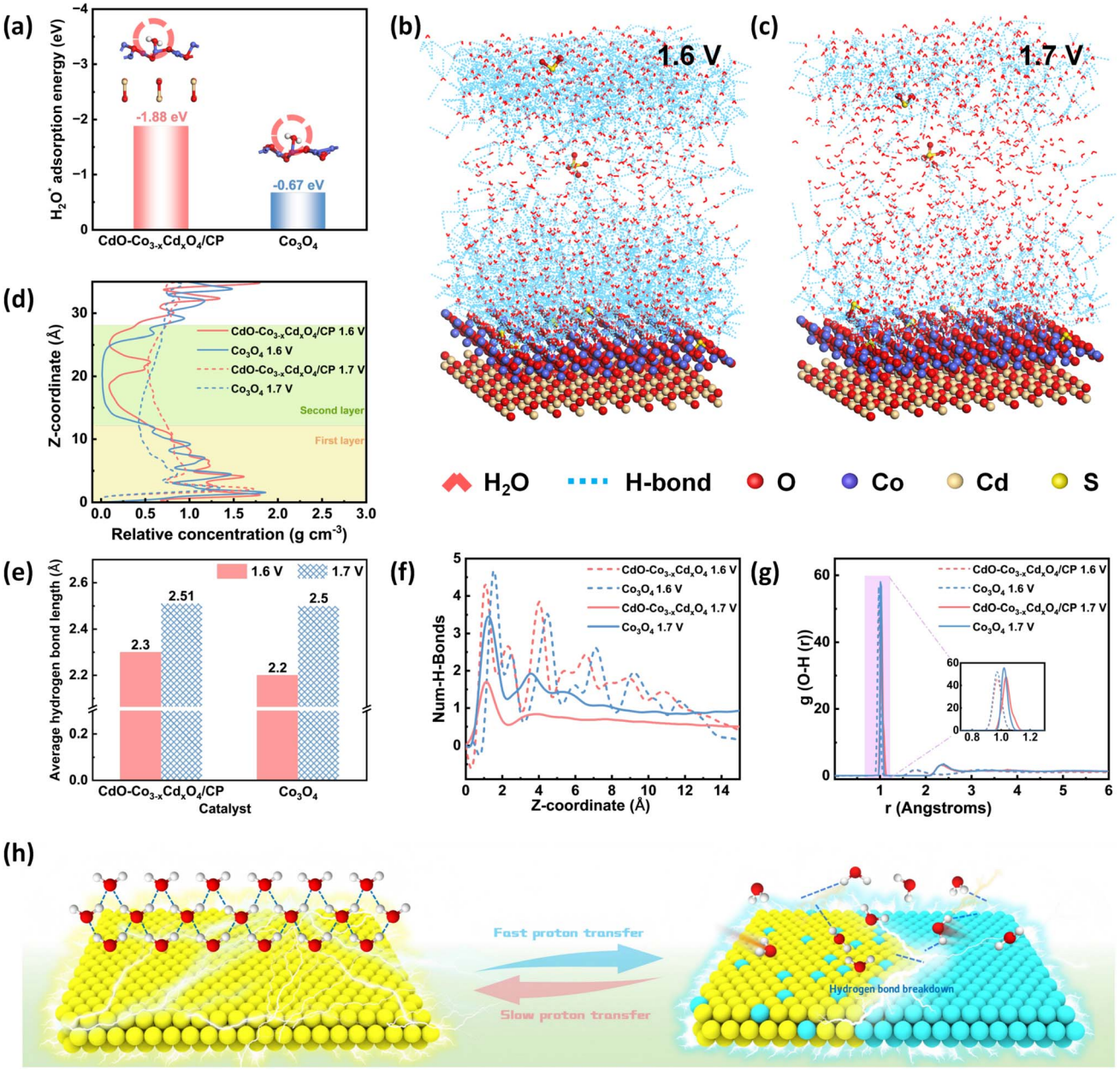

Fig. 4 (a) The binding energies of H_2O on CdO–$Co_{3-x}Cd_xO_4$ and Co_3O_4. (b) Representative snapshots with the H-bond of the interfacial water substructure of CdO–$Co_{3-x}Cd_xO_4$ at 1.6 V and (c) 1.7 V. (d) The relative concentration distribution of CdO–$Co_{3-x}Cd_xO_4$ and Co_3O_4 with respect to the *Z* axis. (e) The average hydrogen bond length per interfacial water molecule for CdO–$Co_{3-x}Cd_xO_4$ and Co_3O_4 models. (f) The corresponding average distribution of the hydrogen bond number along the CdO–$Co_{3-x}Cd_xO_4$ and Co_3O_4 surfaces. (g) The RDF $g_{O-H}(r)$ between O and H atoms of the water interface at 1.6 V and 1.7 V. (h) Schematic diagram illustrating the differing effects of single-phase structures and heterostructures on interfacial water.

that the OER process on both surfaces proceeds *via* a PCET mechanism where proton transfer is kinetically relevant. However, a quantitative analysis reveals a striking divergence in their kinetic behaviors under high-potential conditions. As illustrated in Fig. 3g, at 1.6 V, the KIE value for the heterostructure is 1.1 units higher than that of single-phase Co_3O_4. Crucially, as the potential increases to 1.7 V—where the disruption of the H-bond network is most pronounced—this difference amplifies significantly, with the KIE gap widening to 1.85. This unusually high KIE in the highly active CdO–$Co_{3-x}Cd_xO_4$ heterostructure offers profound mechanistic insight. This suggests that the reaction on the heterostructure surface has shifted to a regime that is highly sensitive to proton transfer dynamics.[45] In contrast, the lower KIE on Co_3O_4 implies that its reaction rate is likely limited by other steps because the rigid H-bond network severely restricts the availability of protons, forcing the reaction to proceed *via* a sluggish, less isotope-sensitive pathway. Combining these results with the *operando* ATR-SEIRAS findings (which showed a surge in isolated water molecules), we propose a refined kinetic model: the

heterostructure-induced electric field disrupts the rigid tetrahedral water network, creating an interface populated with isolated water molecules.

To unravel the atomistic origin of the observed interfacial phenomenon, we performed density functional theory (DFT) calculations and *ab initio* molecular dynamics (AIMD) simulations. First, the binding energy of a water molecule on the CdO–$Co_{3-x}Cd_xO_4$ heterostructure was calculated to be more negative than on Co_3O_4 (Fig. 4a), indicating a stronger affinity for water adsorption. The charge density difference in CdO–$Co_{3-x}Cd_xO$ further reveals the direction of electron transfer within the catalyst, where yellow and blue regions represent electron accumulation and depletion respectively (Fig. S32). Electrons redistribute at the interface within the CdO–$Co_{3-x}Cd_xO$ heterostructure, leading to an elevated oxidation state of Co at the interface.

We then conducted AIMD simulations at 1.6 V and 1.7 V to visualize the interfacial water structure. The representative snapshots and the relative concentration distribution of water molecules along the *Z*-axis (Fig. 4b, c and S33) revealed that at low potential, the water molecules near the catalytic layer interact with the catalytic site to form the first layer of chemisorbed H_2O, and the second layer of water molecules above the first layer interacts with the first layer of water molecules, but the direct interaction with the surface of the catalytic layer is weak and is also affected by the first layer of water molecules. The water molecules in the other layers above the second layer are bulk water molecules. With the increase in potential, the density of the first layer of water decreased slightly, while the density of the second layer of water increased significantly, the water molecules moved upward, and the hydrogen bond network was destroyed. To observe the distribution of water molecules more clearly, Fig. S34 and 4d show the representative snapshot without hydrogen bonds and the distribution of water molecules on the surface of the two catalysts at different potentials. Beyond visual snapshots, we quantitatively analyzed the H-bond network. The calculated average number of H-bonds per water molecule at the interface of CdO–$Co_{3-x}Cd_xO_4$ was significantly lower than that at the Co_3O_4 interface, especially at 1.7 V (Fig. S35). Furthermore, the average H-bond length at the heterostructure interface became longer at high potential (Fig. 4e), indicating weaker and more easily broken H-bonds. The distribution of the H-bond number along the *Z*-axis (Fig. 4f) further confirmed the pervasive disruption of the H-bond network throughout the interfacial region on CdO–$Co_{3-x}Cd_xO_4$. This disrupted network has direct kinetic consequences. The radial distribution function (RDF) $g_{O-H}(r)$ (Fig. 4g) showed a lower peak intensity for CdO–$Co_{3-x}Cd_xO_4$, indicating a less ordered and weaker O–H interaction, which facilitates proton dissociation.[20,46] This finding was corroborated by the RDFs of O–O and H–H (Fig. S36).

In summary, our theoretical simulation provides a new atomic-scale mechanism: the unique electronic structure of the CdO–$Co_{3-x}Cd_xO_4$ heterointerface, characterized by an internal electric field and interfacial forces, shifts the interfacial water to a more disordered state. At high anodic potentials, this effect is dramatically amplified, leading to a significant breakdown of the H-bond network. This breakdown, quantified by a reduced number and longer length of H-bonds, creates a fluidic interface that drastically lowers the barrier for proton dissociation and transport, thereby explaining the potential-dependent performance enhancement.

Conclusion

In summary, this study moves beyond the traditional electronic-structure-based design paradigm by establishing the integrity of the interfacial hydrogen-bond network as a critical kinetic determinant for acidic OER under high-potential conditions. Using the CdO–$Co_{3-x}Cd_xO_4$ heterostructure as a model system, we successfully decoupled the contributions of interfacial water dynamics from bulk electronic effects. Our integrated approach, combining *in situ* ATR-SEIRAS, EIS, and AIMD simulations, provides direct evidence that the heterostructure-induced internal electric field effectively disrupts the interface water network at high anodic potentials. Specifically, we demonstrate that the disruption of the rigid hydrogen-bond network is not merely a structural change, but a prerequisite for unlocking efficient proton transfer pathways. This structural perturbation creates a microenvironment rich in isolated water molecules, which significantly lowers the energy barrier for proton transfer—a bottleneck explicitly confirmed by kinetic isotope effect (KIE) analysis. Ultimately, this work highlights that achieving high-rate water splitting requires a dual focus: we must not only optimize the solid catalyst itself but also engineer the interfacial water environment to ensure rapid proton transport.

Conflicts of interest

The authors declare no competing financial interests.

Author contributions

Xiaolong Liang: conceptualization, data curation, formal analysis, writing-original draft preparation and editing. Jing Liang: investigation, formal analysis. Henkun Yu: formal analysis. Xu Ge: investigation, formal analysis. Ke Xu: analysis and methodology. Yuanjiao Li: resources, testing. Xueliang Mu: resources, testing. Shaoke Zhang: writing-review. Jake M. Yang: writing-review and editing. Jinxuan Liu: conceptualization, resources, methodology, supervision, funding acquisition, writing-review and editing.

Data availability

The data that support the findings of this study are available from the corresponding author upon reasonable request.

Supplementary information (SI): experimental details, supported structure characterization, and catalytic analysis (PDF). See DOI: https://doi.org/10.1039/d6sc01336h.

Acknowledgements

This work was financially supported by the National Natural Science Foundation of China (22272018, U24A20499, and 22088102), Liaoning Binhai Laboratory (LBLD-2024-05), the National Key R&D Program of China (2022YFA0911904), the Fundamental Research Funds for the Central Universities of China (DUT23LAB611 and DUT25YG240) and the State Key Laboratory of Fine Chemicals, Dalian University of Technology (KF2401). The authors acknowledge the assistance of the DUT Instrumental Analysis Center.

References

1 R. Ram, L. Xia, H. Benzidi, A. Guha, V. Golovanova, A. Garzón Manjón, D. Llorens Rauret, P. Sanz Berman, M. Dimitropoulos, B. Mundet, E. Pastor, V. Celorrio, C. A. Mesa, A. M. Das, A. Pinilla-Sánchez, S. Giménez, J. Arbiol, N. López and F. P. García de Arquer, Water-hydroxide trapping in cobalt tungstate for proton exchange membrane water electrolysis, *Science*, 2024, **384**, 1373–1380.

2 P. Li, Y. Jiang, Y. Hu, Y. Men, Y. Liu, W. Cai and S. Chen, Hydrogen bond network connectivity in the electric double layer dominates the kinetic pH effect in hydrogen electrocatalysis on Pt, *Nat. Catal.*, 2022, **5**, 900–911.

3 S. Chu and A. Majumdar, Opportunities and challenges for a sustainable energy future, *Nature*, 2012, **488**, 294–303.

4 J. Liang, X. Gao, K. Xu, J. Lu, D. Liu, Z. Zhao, E. C. M. Tse, Z. Peng, W. Zhang and J. Liu, Unraveling the Asymmetric O-O Radical Coupling Mechanism on Ru-O-Co for Enhanced Acidic Water Oxidation, *Small*, 2023, **19**, e2304889.

5 L. Wang, H. Su, Z. Zhang, J. Xin, H. Liu, X. Wang, C. Yang, X. Liang, S. Wang, H. Liu, Y. Yin, T. Zhang, Y. Tian, Y. Li, Q. Liu, X. Sun, J. Sun, D. Wang and Y. Li, Co-Co Dinuclear Active Sites Dispersed on Zirconium-doped Heterostructured Co_9S_8/Co_3O_4 for High-current-density and Durable Acidic Oxygen Evolution, *Angew. Chem., Int. Ed.*, 2023, **62**, e202314185.

6 Y. Liu, Y. Huang, D. Wu, H. Jang, J. Wu, H. Li, W. Li, F. Zhu, M. G. Kim, D. Zhou, X. Xi, Z. Lei, Y. Zhang, Y. Deng, W. Yan, M. D. Gu, J. Jiang, S. Jiao and R. Cao, Ultrathin and Conformal Depletion Layer of Core/Shell Heterojunction Enables Efficient and Stable Acidic Water Oxidation, *J. Am. Chem. Soc.*, 2024, **146**, 26897–26908.

7 J. Liang, Y. Zhao, C. Yang, S. Zhu, L. Wang, K. Xu, X. Mu, Y. Han, Z. Liu, Z. Zhao, W. Liu, F. Li, Z. Peng, E. C. M. Tse, Q. Liu, J. Gao, Q. Li, J. Li and J. Liu, Dual-Site Cobalt-Doped RuO_2/TiO_2 Electrocatalyst Enables Stable and Cost-Efficient Acidic Oxygen Evolution for PEM Water Electrolysis, *J. Am. Chem. Soc.*, 2025, **147**, 39781–39795.

8 A. Li, S. Kong, C. Guo, H. Ooka, K. Adachi, D. Hashizume, Q. Jiang, H. Han, J. Xiao and R. Nakamura, Enhancing the stability of cobalt spinel oxide towards sustainable oxygen evolution in acid, *Nat. Catal.*, 2022, **5**, 109–118.

9 S. Pan, H. Li, D. Liu, R. Huang, X. Pan, D. Ren, J. Li, M. Shakouri, Q. Zhang, M. Wang, C. Wei, L. Mai, B. Zhang, Y. Zhao, Z. Wang, M. Graetzel and X. Zhang, Efficient and stable noble-metal-free catalyst for acidic water oxidation, *Nat. Commun.*, 2022, **13**, 2294.

10 X. Zhang, C. Feng, B. Dong, C. Liu and Y. Chai, High-Voltage-Enabled Stable Cobalt Species Deposition on MnO_2 for Water Oxidation in Acid, *Adv. Mater.*, 2023, **35**, e2207066.

11 M. Blasco-Ahicart, J. Soriano-López, J. J. Carbó, J. M. Poblet and J. R. Galan-Mascaros, Polyoxometalate electrocatalysts based on earth-abundant metals for efficient water oxidation in acidic media, *Nat. Chem.*, 2018, **10**, 24–30.

12 J.-H. Kim, D. H. Youn, K. Kawashima, J. Lin, H. Lim and C. B. Mullins, An active nanoporous Ni(Fe) OER electrocatalyst *via* selective dissolution of Cd in alkaline media, *Appl. Catal., B*, 2018, **225**, 1–7.

13 Z. Liu, W. Shen, X. Liang, J. Liang, K. Xu, X. Ge, J. Lu, H. Liu, J. Xiao, L. Wang, J. Gao and J. Liu, Dual-Regulation Engineering of Spinel Co_3O_4 *via* Mo Electron Buffering and Asymmetric Sites Coupling for Acidic Oxygen Evolution Reaction, *ACS Catal.*, 2025, **15**, 8943–8953.

14 C. Rong, K. Dastafkan, Y. Wang and C. Zhao, Breaking the Activity and Stability Bottlenecks of Electrocatalysts for Oxygen Evolution Reactions in Acids, *Adv. Mater.*, 2023, **35**, e2211884.

15 J. Liu, T. Wang, X. Liu, H. Shi, S. Li, L. Xie, Z. Cai, J. Han, Y. Huang, G. Wang and Q. Li, Reducible Co^{3+}–O Sites of Co–Ni–P–O_x on CeO_2 Nanorods Boost Acidic Water Oxidation *via* Interfacial Charge Transfer-Promoted Surface Reconstruction, *ACS Catal.*, 2023, **13**, 5194–5204.

16 N. Wang, P. Ou, R. K. Miao, Y. Chang, Z. Wang, S. F. Hung, J. Abed, A. Ozden, H. Y. Chen, H. L. Wu, J. E. Huang, D. Zhou, W. Ni, L. Fan, Y. Yan, T. Peng, D. Sinton, Y. Liu, H. Liang and E. H. Sargent, Doping Shortens the Metal/Metal Distance and Promotes OH Coverage in Non-Noble Acidic Oxygen Evolution Reaction Catalysts, *J. Am. Chem. Soc.*, 2023, **145**, 7829–7836.

17 Z. W. Seh, J. Kibsgaard, C. F. Dickens, I. Chorkendorff, J. K. Norskov and T. F. Jaramillo, Combining theory and experiment in electrocatalysis: Insights into materials design, *Science*, 2017, **355**, eaad4998.

18 T. Zhang, Q. Ye, Z. Han, Q. Liu, Y. Liu, D. Wu and H. J. Fan, Biaxial strain induced OH engineer for accelerating alkaline hydrogen evolution, *Nat. Commun.*, 2024, **15**, 6508.

19 C. Y. Li, J. B. Le, Y. H. Wang, S. Chen, Z. L. Yang, J. F. Li, J. Cheng and Z. Q. Tian, In situ probing electrified interfacial water structures at atomically flat surfaces, *Nat. Mater.*, 2019, **18**, 697–701.

20 A. H. Shah, Z. Zhang, Z. Huang, S. Wang, G. Zhong, C. Wan, A. N. Alexandrova, Y. Huang and X. Duan, The role of alkali metal cations and platinum-surface hydroxyl in the alkaline hydrogen evolution reaction, *Nat. Catal.*, 2022, **5**, 923–933.

21 I. Popov, Z. Zhu, A. R. Young-Gonzales, R. L. Sacci, E. Mamontov, C. Gainaru, S. J. Paddison and A. P. Sokolov, Search for a Grotthuss mechanism through the observation of proton transfer, *Commun. Chem.*, 2023, **6**, 77.

22 L. Wang, Y. Hao, J. Pan, S. Bi, S.-F. Hung, K.-S. Peng, A.-Y. Wang, T.-Y. Chen, S. Li, C. Ling, Y. Zhang, L. Li, F. Hu, X. Zhou, H.-Y. Chen, K. Wu, J. Wang, Y. Wu and S. Peng, Tailored water–surface interactions on cobalt

oxide for stable proton-exchange-membrane water electrolysis, *Nat. Catal.*, 2026, **9**, 123–133.

23 X. Chen, X. T. Wang, J. B. Le, S. M. Li, X. Wang, Y. J. Zhang, P. Radjenovic, Y. Zhao, Y. H. Wang, X. M. Lin, J. C. Dong and J. F. Li, Revealing the role of interfacial water and key intermediates at ruthenium surfaces in the alkaline hydrogen evolution reaction, *Nat. Commun.*, 2023, **14**, 5289.

24 X. You, D. Zhang, X. G. Zhang, X. Li, J. H. Tian, Y. H. Wang and J. F. Li, Exploring the Cation Regulation Mechanism for Interfacial Water Involved in the Hydrogen Evolution Reaction by *In Situ* Raman Spectroscopy, *Nano-Micro Lett.*, 2023, **16**, 53.

25 J. Shan, C. Ye, S. Chen, T. Sun, Y. Jiao, L. Liu, C. Zhu, L. Song, Y. Han, M. Jaroniec, Y. Zhu, Y. Zheng and S.-Z. Qiao, Short-Range Ordered Iridium Single Atoms Integrated into Cobalt Oxide Spinel Structure for Highly Efficient Electrocatalytic Water Oxidation, *J. Am. Chem. Soc.*, 2021, **143**, 5201–5211.

26 J. Qian, X. Liu, C. Zhong, G. Xu, H. Li, W. Zhou, B. You, F. Wang, D. Gao and D. Chao, Enhanced Stability and Narrowed D-Band Gap of Ce-Doped Co_3O_4 for Rechargeable Aqueous Zn-Air Battery, *Adv. Funct. Mater.*, 2022, **33**, 2212021.

27 D. Bao, L. Huang, Y. Zheng and S.-Z. Qiao, Lattice Strain-Induced Regulation of Interfacial Water Promotes Hydrogen Production from Natural Seawater, *ACS Catal.*, 2025, **15**, 14661–14670.

28 X. Kang, X. J. Yang, Z. Meng, X. F. Sun, M. M. Shi, H. R. Li, R. Gao, B. Bi, D. X. Liu, J. M. Yan and Q. Jiang, Self-Supported Catalytic Electrode of CoW/Co-Foam Achieves Efficient Ammonia Synthesis at Ampere-Level Current Density, *Adv. Energy Mater.*, 2023, **14**, 2303321.

29 T.-T. Yang, M. Wang, F.-F. Zhang, C. Xi, L. Xiao, X. Zhao, J. Wang, W. Hua, C.-K. Dong, H. Liu and X.-W. Du, Immiscible Ruthenium–Cadmium Alloy for Acidic Oxygen Evolution Reaction, *ACS Energy Lett.*, 2024, **9**, 3955–3961.

30 Y. Lu, C. L. Dong, Y. C. Huang, Y. Zou, Z. Liu, Y. Liu, Y. Li, N. He, J. Shi and S. Wang, Identifying the Geometric Site Dependence of Spinel Oxides for the Electrooxidation of 5-Hydroxymethylfurfural, *Angew. Chem., Int. Ed.*, 2020, **59**, 19215–19221.

31 Z. Xiao, Y.-C. Huang, C.-L. Dong, C. Xie, Z. Liu, S. Du, W. Chen, D. Yan, L. Tao, Z. Shu, G. Zhang, H. Duan, Y. Wang, Y. Zou, R. Chen and S. Wang, Operando Identification of the Dynamic Behavior of Oxygen Vacancy-Rich Co_3O_4 for Oxygen Evolution Reaction, *J. Am. Chem. Soc.*, 2020, **142**, 12087–12095.

32 H.-Y. Wang, S.-F. Hung, H.-Y. Chen, T.-S. Chan, H. M. Chen and B. Liu, Operando Identification of Geometrical-Site-Dependent Water Oxidation Activity of Spinel Co_3O_4, *J. Am. Chem. Soc.*, 2015, **138**, 36–39.

33 N. Zhang, Y. Hu, L. An, Q. Li, J. Yin, J. Li, R. Yang, M. Lu, S. Zhang, P. Xi and C. H. Yan, Surface Activation and Ni-S Stabilization in NiO/NiS_2 for Efficient Oxygen Evolution Reaction, *Angew. Chem., Int. Ed.*, 2022, **61**, e202207217.

34 K. Tong, L. Xu, H. Yao, X. Wang, C. Zhang, F. Yang, L. Chu, J. Lee, H. Jiang and M. Huang, Hydrogen spillover bridged dual nano-islands triggered by built-in electric field for efficient and robust alkaline hydrogen evolution at ampere-level current density, *Nano Res.*, 2024, **17**, 5050–5060.

35 X. Tong, Y. Zhao, Z. Zhuo, Z. Yang, S. Wang, Y. Liu, N. Lu, H. Li and T. Zhai, Dual-Regulation of Defect Sites and Vertical Conduction by Spiral Domain for Electrocatalytic Hydrogen Evolution, *Angew. Chem., Int. Ed.*, 2021, **61**, e202112953.

36 X. Zhao, Z. Li, H. Jang, X. Wei, L. Wang, M. G. Kim, J. Cho, X. Liu and Q. Qin, 2D Ruthenium–Chromium Oxide with Rich Grain Boundaries Boosts Acidic Oxygen Evolution Reaction Kinetics, *Small*, 2024, **20**, 2311172.

37 S. Zhao, S.-F. Hung, L. Deng, W.-J. Zeng, T. Xiao, S. Li, C.-H. Kuo, H.-Y. Chen, F. Hu and S. Peng, Constructing regulable supports *via* non-stoichiometric engineering to stabilize ruthenium nanoparticles for enhanced pH-universal water splitting, *Nat. Commun.*, 2024, **15**, 2728.

38 S. Li, L. Wu, Q. Liu, M. Zhu, Z. Li, C. Wang, X. Jiang and J. Li, Uncovering the Dominant Role of an Extended Asymmetric Four-Coordinated Water Network in the Hydrogen Evolution Reaction, *J. Am. Chem. Soc.*, 2023, **145**, 26711–26719.

39 X. Yang, H. Ding, S. Li, S. Zheng, J.-F. Li and F. Pan, Cation-Induced Interfacial Hydrophobic Microenvironment Promotes the C–C Coupling in Electrochemical CO_2 Reduction, *J. Am. Chem. Soc.*, 2024, **146**, 5532–5542.

40 Y. Liu, Z. Zhuang, Y. Liu, N. Liu, Y. Li, Y. Cheng, J. Yu, R. Yu, D. Wang and H. Li, Shear-Strained Pd Single-Atom Electrocatalysts for Nitrate Reduction to Ammonia, *Angew. Chem., Int. Ed.*, 2024, **63**, e202411396.

41 J. Yang, J. Jiao, S. Liu, Y. Yin, Y. Cheng, Y. Wang, M. Zhou, W. Zhao, X. Tong, L. Jing, P. Zhang, X. Sun, Q. Zhu, X. Kang and B. Han, Switching Reaction Pathways of CO_2 Electroreduction by Modulating Cations in the Electrochemical Double Layer, *Angew. Chem., Int. Ed.*, 2024, **63**, e202410145.

42 Y. Duan, L. L. Wang, W. X. Zheng, X. L. Zhang, X. R. Wang, G. J. Feng, Z. Y. Yu and T. B. Lu, Oxyanion Engineering on RuO_2 for Efficient Proton Exchange Membrane Water Electrolysis, *Angew. Chem., Int. Ed.*, 2024, **63**, e202413653.

43 L. Deng, H. Chen, S.-F. Hung, Y. Zhang, H. Yu, H.-Y. Chen, L. Li and S. Peng, Lewis Acid-Mediated Interfacial Water Supply for Sustainable Proton Exchange Membrane Water Electrolysis, *J. Am. Chem. Soc.*, 2024, **146**, 35438–35448.

44 Y. Yang, R. G. Agarwal, P. Hutchison, R. Rizo, A. V. Soudackov, X. Lu, E. Herrero, J. M. Feliu, S. Hammes-Schiffer, J. M. Mayer and H. D. Abruña, Inverse kinetic isotope effects in the oxygen reduction reaction at platinum single crystals, *Nat. Chem.*, 2022, **15**, 271–277.

45 J. Huang, R. Wang, H. Sheng, X. Zhu, R. Dominic Ross, D. Hua, L. Lin, Y. Li, Q. Zhang, L. Gu, X. Wang, P. Xu, J. Lu, S. Jiang, J. Han, B. Song and S. Jin, Isotope-dependent Tafel analysis probes proton transfer kinetics during electrocatalytic water splitting, *Nat. Chem.*, 2025, DOI: 10.1038/s41557-025-01934-5.

46 Z. Yang, L. Chen, Y. Yin, C. Wei, Z. Xue and T. Mu, Weakened hydrogen bond connectivity promotes interfacial mass transfer for industrial level scalable biomass electrooxidation, *Energy Environ. Sci.*, 2024, **17**, 8801–8809.